Inkjet Printing of Sc-Doped TiO$_2$ with Enhanced Photoactivity

Kirill Keller [1,*,†] , **Elena V. Khramenkova** [1,2,†], **Vladislav Slabov** [1,†], **Albina Musin** [3], **Alexander Kalashnikov** [4], **Alexandr V. Vinogradov** [1,*] and **Evgeny A. Pidko** [1,5]

1   Department of Chemistry and Molecular Biology, ITMO University, St. Petersburg 191002, Russia; khramenkova@scamt-itmo.ru (E.V.K.); slabov@scamt-itmo.ru (V.S.); e.a.pidko@tudelft.nl (E.A.P.)
2   Department of Chemical Engineering and Chemistry, Eindhoven University of Technology, 5600 Eindhoven, The Netherlands
3   Department of Physics, Ariel University, Ariel 4635, Israel; albinam@ariel.ac.il
4   Rock Capital Partners, 101000 Moscow, Russia; alexander.kalashnikov@gmail.com
5   Department of Chemical Engineering, Delft University of Technology, 2628 Delft, The Netherlands
*   Correspondence: kellertab@gmail.com (K.K.); avv@scamt-itmo.ru (A.V.V.)
†   These authors contributed equally to this study.

Abstract: Here we report the methodology for nanocomposite fabrication based on the inkjet printing technique. Doped TiO$_2$ nanoparticles with Sc contents up to 10 wt.% were synthesized and adapted towards a facile fabrication of microscale structures and thin film printing. Implementation of the state-of-the-art low-temperature synthesis allowed to us successfully incorporate high concentrations of Sc^{3+} ions into the TiO$_2$ lattice and improve the light absorption characteristics of the resulting materials. Without affecting the anatase structure substantially, Sc doping gave rise to an intensified absorbance capacity and provided the means for the efficient fabrication of Sc-TiO$_2$ microarchitectures via the inkjet printing technique. The changes in the spectral and structural characteristics of the Sc-TiO$_2$ composites were observed by Energy Dispersive X-Ray spectroscopy (EDX), X-ray diffraction (XRD), and UV-vis methods. The rheological parameters of the colloidal suspension based on the synthesized Sc-TiO$_2$ nanoparticles were adapted for inkjet printing in terms of the optimal viscosity, morphology, and surface tension. The developed individual ink characteristics allowed us to produce a close coherence between the enhanced optical properties of the Sc-TiO$_2$ prepared the sol–gel method and the inkjet-printed films. The introduced methodology features the possibility to inkjet-print doped and pure TiO$_2$ robust films for potential large-scale fabrication.

Keywords: inkjet printing; DFT; TiO$_2$

1. Introduction

Access to alternative energy sources is the key factor that enables sustainable development strategies and environmentally friendly energy technologies [1,2]. In this context, engineering materials with desirable characteristics and the scale-up of their production to the industrial level are crucial manufacturing stages. Among different technologies for the manufacturing of nanostructured and composite materials, inkjet printing has recently attracted increasing attention both in industry and in academia as it allows for a substantial reduction of the number of necessary technological steps by enabling controlled multiphase depositions, while also ensuring high material economy, process speed, and accuracy of the deposition process [3–5]. Inkjet printing is based on the ejection of a colloidal suspension on the surface of choice with the formation of bulk micro- and submicron three-dimensional (3D)-structures [6]. Inkjet printing offers both the possibility to construct materials and devices from

scratch and can be employed as a supplementary stage in the fabrication of complex 3D-architectures. Inkjet printing is a flexible and versatile additive manufacturing technique suitable both for thin film and microrelief production, well adapted for laboratory and industry applications [7–9]. It can be used for precise deposition with an accuracy of 1–2 µm. Moreover, inkjet printing does not require a physical template or mask, which is an advantage over spin-coating, lithography, and spraying approaches [10–12]. Being controlled by a computer, the high printing accuracy along with the availability of the various substrates significantly simplify the technology and facilitate the production of complex heterostructures [13,14].

Solar cells play an important role in the alternative energy sector, as they directly convert abundant solar energy to electricity. During the past decades, numerous studies have been devoted to improving solar cell performance and lowering the price of this technology [15]. One of the widely explored approaches involves the use of the thin film multijunction solar cell. Such a composite architecture combines the efficient photon conversion to electrons and their transport from multiple layers, each absorbing different wavelengths of light. It has been shown that semiconductor absorption capacity is a critical controllable parameter influencing the overall efficiency of a solar cell [16,17].

One of the most widely used and extensively explored semiconductors is TiO_2. Various approaches have been explored so far to improve the photochemical characteristics of TiO_2 [18–20], among which structural doping is one of the most widely used methods to shift light absorption to the visible region and enhance the overall performance of TiO_2-based composites. Previously, doping the TiO_2 structure with various metals (Fe, Mn, Sc, V, Cr, Mn) and non-metals (N, C, F, S) [21–23] has been considered as an approach to enhance the photosensitivity of the TiO_2 nanoparticles at lower wavelengths and, particularly, in the visible spectral range.

In this work, we aimed to optimize the inkjet printing process of titania-based nanocomposite thin film fabrication, placing an emphasis on its photoabsorption characteristics influenced by doping agents [16,17,24]. Scandium was chosen as a dopant for its ability to cause a photoabsorption shift into the visible region [25,26]. For this purpose, we synthesized a range of Sc-doped TiO_2 nanoparticles with up to 10 wt.% Sc incorporation using a novel sol–gel approach and we inkjet-printed the thin films out of a colloidal suspension, applying optimized rheological parameters. The similar ionic radii of Sc^{3+} and Ti^{4+} cations facilitate the doping process (which is effectively the substitution of the lattice centers) without substantially affecting the structure of the original material [27]. The sol–gel synthesis procedure described in this work allowed us to substantially increase the degree of Sc^{3+} incorporation into the TiO_2 structure as compared to earlier reports [28]. All the synthesized materials were comprehensively characterized by SEM, TEM, X-ray diffraction (XRD), and UV-Vis methods, while the adaptation of their rheological parameters made them ready for inkjet printing. Among the potential drawbacks of the inkjet process of multicomponent systems are phase separation and coffee-ring formation [29]. These problems were profoundly studied in previously works [30,31]; thus, in the present work we found optimal printing parameters and drying conditions for uniform film deposition in order to prevent the abovementioned challenges.

The choice of Sc as the doping agent was additionally rationalized by periodic density functional theory (DFT) calculations that gave evidence of the facile incorporation of Sc^{3+} in the anatase structure, resulting in the desired changes of the electronic properties of the final composite material.

2. Materials and Methods

2.1. Materials and Characterization Methods

A non-hydrothermal synthesis of Sc-TiO_2 nanoparticles was performed using the following reagents: scandium (III) nitrate (99.9%), nitric acid (65%), titanium isopropoxide (99%), and isopropanol. The resulting inks were prepared on the base of synthesized pure and Sc-doped TiO_2 nanoparticles dispersed in ethylene glycol (purity 99%) with such dispersants as the surfactant Dynax DX4000.

All reagents were obtained from Sigma-Aldrich Rus (Moscow, Russia) and were used as received without further purification. Deionized water was used in all experimental procedures.

Particle sizes and the zeta potential of pure and doped TiO_2 nanoparticles were measured using a Photocor Compact-Z analyzer (Moscow, Russia) at 25 °C. Measurements of rheological properties were carried out using a rotational viscometer Fungilab Expert (Barcelona, Spain) with a small sample adapter APM. The surface tension of the produced inks was measured on a drop shape KRÜSS DSA-25 analyzer (Hamburg, Germany). The morphology of the printed drops was obtained using SEM Tescan Vega 3 (Kohoutovice, Czech Republic). TEM measurements of synthesized samples were performed on an FEI Talos F200X (Hillsboro, OR, USA) at an operating voltage of 200 kV. XRD analysis was performed with a Rigaku SmartLab 3 X-ray diffractometer (Tokyo, Japan) using a Cu-Kα source (λ = 1.54 Å). Samples were scanned at a rate of 1 degree per minute. Optical absorbance spectra of synthesized powders were measured on a Perkin Elmer Lambda 1050 UV-Vis spectrophotometer (Akron, OH, USA) in diffuse reflectance mode and IR absorbance were measured on a Thermo Scientific Nicolet 8700 IR-Fourier spectrometer (Waltham, MA, USA). Inkjet-printed films were analyzed with an Agilent Cary 60 UV-Vis spectrophotometer in specular reflectance mode using a film sample holder. Optical microscopy images were made with a Hirox RH-2000 Digital Microscope (Hackensack, NJ, USA). The specific surface area was investigated using a Quantachrome Nova 1200e (Boynton Beach, FL, USA) by nitrogen adsorption at 77 K and analyzed using the BET (Brunauer–Emmett–Teller) and BJH (Barrett-Joyner-Halenda) equations.

Ink deposition was performed on a Dimatix Materials printer DMP 2831 (Santa Clara, CA, USA) with a 10 pL cartridge. The printing procedure was carried out with a jetting frequency of 5 kHz, and the voltage on the nozzles was varied in the range of 19 to 21 V. Figure S9 shows the used waveform with detailed information about duration and signal level.

A film on a glass substrate was printed with a drop spacing of 10 μm in four layers and calcinated at 370 °C for 30 min. The drop array was printed on the silicon wafer with a drop spacing of 50 μm, a temperature of 35 °C, and a drop velocity of 8 m s^{-1}.

2.2. Synthesis of Pure and Sc-Doped TiO$_2$ Nanoparticles

Pure and Sc-doped TiO_2 nanoparticles were synthesized using a modified low-temperature peptization procedure previously reported with nitric acid as the peptizing agent [32,33]. Initially, 0.7 mL of 66% HNO_3 and a certain amount of $Sc(NO_3)_3$ (3/5/7/10 wt.%) were mixed in 100 mL of water. The obtained solution was heated to 70 °C under constant intensive stirring with a magnetic stirrer. The next step included the solvation of 7 mL titanium isopropoxide in 12 mL of isopropanol. Upon reaching the desired temperature of 70 °C, the mixture of isopropanol and isopropoxide was added to the heated beaker with an acidic solution of scandium, producing white flakes. Then the system was heated at 80 °C for 45 min. Thereafter, the heat was turned off, the beaker covered with foil, and the contents were stirred for four days.

The obtained colloid solution of doped titania nanoparticles was heated to 40 °C in a rotary evaporator under vacuum until the complete evaporation of the water was achieved. Then, the obtained xerogel of the nanoparticles was collected and triturated for further analyses. No calcination was performed for all experiments.

2.3. Computational Models and Methods

To rationalize the observed the changes in the electronic structure caused by Sc incorporation into the TiO_2 lattice, periodic density functional theory (DFT) calculations were carried out. Periodic models of the anatase polymorph were used to simulate the various concentrations of the dopants in the anatase lattice. A 3 × 3 × 2 supercell was constructed from an anatase unit cell with the optimized lattice parameters (Figure S1). The supercell models with impurities including 5% and 10% Sc^{3+} mass concentrations were simulated by introducing four and eight Ti^{4+} to Sc^{3+} substitutions, respectively (Figure S2). Such a doping procedure generates a charge imbalance that is compensated

by introducing oxygen vacancies [34]. Accordingly, two and four oxygen atoms were removed in the 5% and 10% Sc^{3+}-doped TiO_2 supercells, respectively. X-ray diffraction patterns for the optimized structures were simulated using the VESTA software package [35].

3. Results and Discussions

3.1. Physicochemical Characterization of Sc-Doped Nanoparticles

A series of synthesized Sc-doped TiO_2 nanoparticles with Sc contents varying from 0 to 10 wt.% were synthesized and thoroughly characterized. The synthetic approach used here followed a procedure introduced previously for the sol–gel synthesis of anatase nanoparticles with the addition of a stoichiometric amount of scandium ions. The increase of the concentration of Sc^{3+} ions was accompanied by a decrease of the average hydrodynamic particle diameter as measured by the dynamic light scattering (DLS) method (Figure 1). EDX analysis was performed on small areas and more significant fields of the samples revealed a homogeneous Sc distribution across the nanoparticles in concentrations close to the intended ones (Table 1).
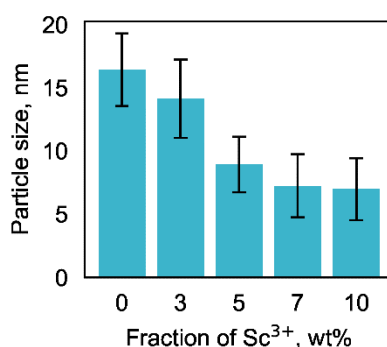
Figure 1. Particle size in obtained colloids of Sc-doped titania.

Table 1. Calculated and EDX amounts of Sc ions in synthesized Sc-doped titanium dioxide.

Sc Calculated, wt.%	Sc Experimental, wt.%
3	2.89 ± 0.15
5	5.34 ± 0.18
7	6.51 ± 0.13
10	9.69 ± 0.09

The phase composition and the crystallinity of the synthesized samples were examined by powder X-ray diffraction (XRD) analysis. The corresponding XRD patterns of the synthesized samples of pure and Sc-doped TiO_2 nanoparticles evidenced a pure anatase phase with a high crystallinity for all samples (Figure 2). The diffractograms clearly showed the efficient embedding of the guest ions in the anatase structure because no additional peaks were detected in the doped materials. No evidence of phase separation was observed.
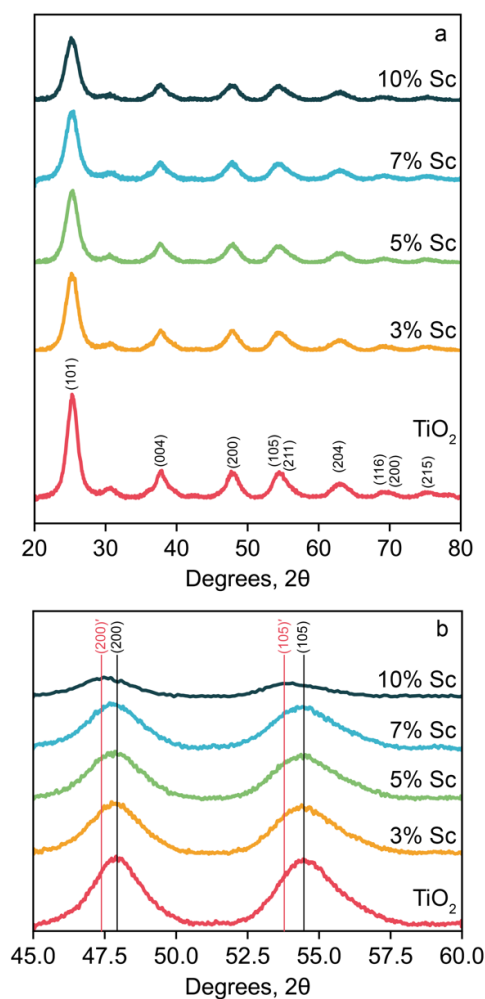
Figure 2. X-ray diffraction (XRD) patterns of pure TiO$_2$ and Sc-doped samples in fields 2θ = 20°–80° (**a**) and 2θ = 45°–60° (**b**).

The incorporation of Sc into the TiO$_2$ lattice resulted in the shift of the (200) and (105) reflections by 0.6° and 0.75°, respectively (Figure 2b). The increase of the Sc content in the samples from 0 to 10 wt.% resulted in uniform shifts of both reflections in the XRD patterns, evidencing a homogeneous incorporation of Sc into the TiO$_2$ lattice that was accompanied only smooth changes in the lattice parameters without substantial structural changes.

To further verify the proposed structural transformations in TiO$_2$ in the presence of Sc, we carried out periodic DFT calculations on model TiO$_2$ structures and their doped counterparts. Our calculations revealed that the substitution of part of Ti with Sc and the formation of oxygen defects led to a distortion of the crystal structure that represented the expansion of the supercell by up to 0.5% along the *a*-axis and up to 2% along the *c*-axis for the model with the highest Sc content (10 wt.%) (see Table S6). The cell expansion was in line with the larger ionic radius of Sc (88.5 pm) compared to that of Ti (74.5 pm). In line with the experimental observations, these structural changes were reflected in minor but notable shifts of the main reflections in the simulated XRD patterns (see Figure S3).

To estimate how the introduction of Sc influences the photoabsorption activity of TiO$_2$, experimental UV-vis measurements of pure and Sc-doped samples were conducted (Figure 3). Besides the extension of the absorption edge to the visible range, the spectra in Figure 3a evidenced a significant increase of the overall absorbance in the UV region. Moreover, the increasing A bandgap is an important characteristic of semiconductors and it can be estimated from Tauc plots based on the observed spectra (Figure 3b). This approach employs a linear approximation of the energy of the

probing radiation $h\nu$ as a function of the semiconductor absorption coefficient α near the fundamental absorption edge [36]. The *x*-axis in the Tauc plots corresponds to $h\nu$ and the *y*-axis gives the $(\alpha h\nu)^{1/n}$, where *n* stands for the transition index [37]. Because anatase is an indirect bandgap semiconductor, its transition index for the indirect forbidden transition was given as $n = 3$. To calculate the absorption coefficient α, we used the Kubelka–Munk equation:

$$\alpha = \frac{(1 - R)^2}{2R} \tag{1}$$
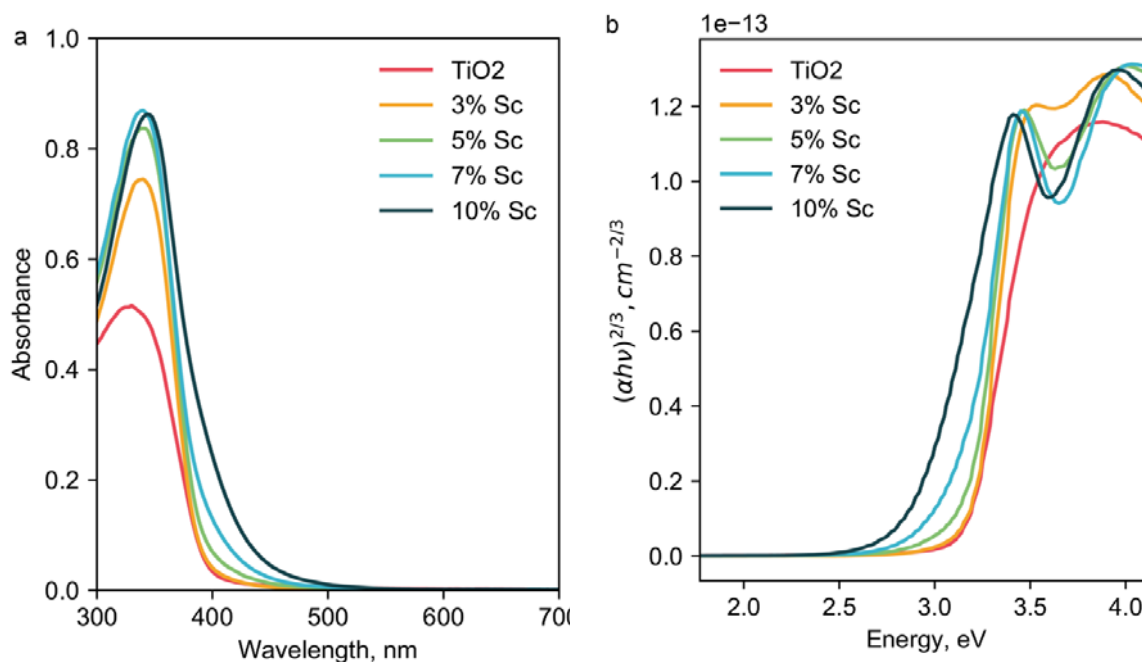
Figure 3. Absorbance spectra of pure and doped samples of TiO_2 (**a**), Tauc plot (**b**).

The values of the forbidden optical bandgaps were derived from the Tauc plots by constructing tangent lines for each sample. The results presented in Table 2 evidence the declining bandgap value with increasing Sc contents. As a result, the absorbance edge shifts into the visible part of the spectrum that agrees perfectly with our theoretical calculations.

Table 2. Experimental values of the optical forbidden bandgap E_g for pure and Sc-doped titania obtained from the Tauc plot.

Sample	E_g, eV	Wavelength, nm
TiO_2	3.2	387.5
TiO_2 + 3% Sc	3.18	389.9
TiO_2 + 5% Sc	3.14	394.9
TiO_2 + 7% Sc	3.11	398.7
TiO_2 + 10% Sc	2.9	427.6

In line with the results of the UV-vis spectroscopy measurements, periodic DFT+U (see Appendix A) calculations also predicted a substantial change in the electronic structure of the doped anatase. The computed bandgap for pure anatase was 3.27 eV, which is in perfect agreement with the experimental value of 3.2 eV [38]. The introduction of Sc into the lattice reduced the bandgap to the values of 2.99 eV and 2.85 eV for 5 wt.% and 10 wt.% Sc-TiO_2, respectively (Table S5). These were translated to the shift of the absorbance maximum in the spectra from 379 nm for pure TiO_2 to 415 nm

and 435 nm for 5 wt.% and 10 wt.%. Sc-TiO$_2$, respectively, rendering these materials appropriate targets for the experimental design of semiconductor materials with improved photochemical characteristics.

The results of the electron microscopy characterization of the pure and Sc-doped TiO$_2$ dried nanoparticles are shown in Figure 4. The comparison of the SEM micrographs for the two materials (Figure 4a,c) implied only a small influence of Sc doping on the morphology of the main crystallites, although pure TiO$_2$ nanoparticles tend to form larger aggregates upon drying. TEM micrographs (Figure 4b,d) also indicated the formation of narrow pores with a diameter below 2 nm, which is in perfect agreement with the results of N$_2$ physisorption (see Supplementary Information).
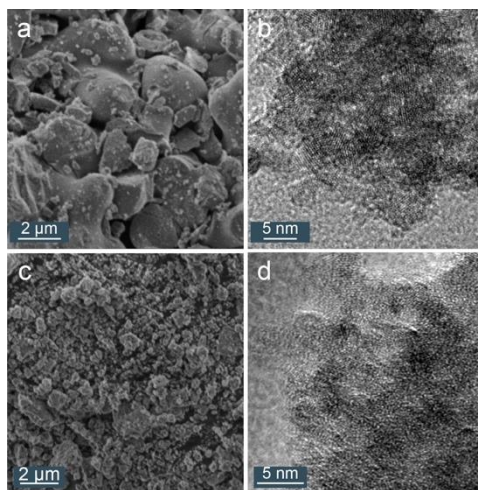
Figure 4. SEM images of pure (**a**) and 10% Sc-doped (**c**) TiO$_2$; TEM images of pure (**b**) and 10% Sc-doped (**d**) TiO$_2$.

3.2. Inkjet Printing

The preparation of inorganic inks for efficient inkjet printing involves—besides the actual synthesis of the stable colloid—the optimization of rheological parameters and filling inks into the cartridge. Because the as-synthesized titanium dioxide is well-dispersive in water and exhibits stable colloid formulation, our primary task was the optimization of the rheological parameters of the inks. The theory of inkjet printing is based on Ohnesorge equations containing the hydrodynamic dimensionless Reynolds and Weber numbers. The Ohnesorge number reflects the physical properties of printability and drop formation. The Reynolds number is a ratio between the inertial and viscous forces in the fluid, while the Weber number demonstrates a ratio between the drop momentum and its surface tension. The critical parameters having the most significant impact on ink printability are viscosity and surface tension.

$$Oh = \frac{\sqrt{We}}{Re} \tag{2}$$

$$Re = \frac{\rho V d}{\eta} \tag{3}$$

$$We = \frac{\rho V^2 d}{\gamma} \tag{4}$$

The viscosity of the water-based sols was adjusted with ethylene glycol. Figure 5a shows the change of the viscosity as a function of the ethylene glycol concentration. This additive was selected in view of its relatively high viscosity (18 cPs) and low vapor pressure as well as its perfect miscibility with water-based colloids that at the same time does not affect the dispersed nanoparticles. To reduce the surface tension of inks, we introduced the cationic surfactant Dynax DX4000 (Tokyo, Japan). Figure 5b shows the evolution of the surface tension with the concentration of the surfactant. Considering the hydrodynamic calculations of composition adjustments, and as

previously reported, it was found that the optimal amount of added surfactant was 20 μL per 1 mL of ethylene glycol and doped titania colloid with a ratio of 2:1, respectively. Because the doping of anatase has no effect on rheology, and its impact on particle size is negligible, the printing parameters and the waveform determined for TiO_2 were used for the doped material as well. To study the ink stability and the impact of additives on the sedimentation, the zeta potential of inks was measured. The results (Figure S10) showed a slight effect of the additives on the stability of the ink, with a zeta-potential higher than 30 mV in all cases. The inks were prepared for 10 wt.% Sc-TiO_2 and the final ink parameters are summarized in Table 3.
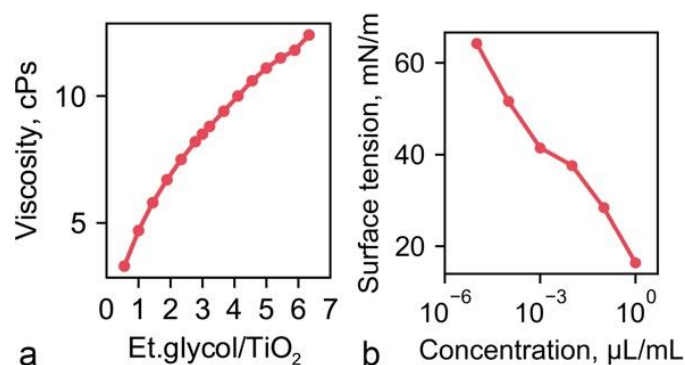
Figure 5. Rheological parameters of inks: viscosity curve of ethylene glycol/water colloid of titania nanoparticles (**a**), values of surface tension under different surfactant concentrations (**b**).

Table 3. Main parameters of the prepared inks.

Surface Tension, mN/m	Viscosity, cPs	Particle Size, nm	Z-Number
28	6.7	8.4	4.2

In this work, a cartridge with a drop volume of 10 pL was used. Before filling the cartridge, the ink was filtered with a syringe filter featuring a 220-nm membrane followed by degassing for 30 min. These procedures were performed to avoid larger particles and air bubbles in the nozzle that could affect the printing accuracy and performance. Figure 6a,b show SEM images of the printed 10 wt.% Sc-TiO_2 drops, evidencing their highly uniform deposition at an equal distance of 120 μm (center-to-center) with no traces of satellite droplets. With variation of the drop spacing and a number of printed layers, a film with a defined uniformity and thickness can be achieved. Figure 6c,e present a film on a glass substrate printed in four layers. The images show even particle distribution and a low film roughness. The film had a thickness of 0.8 μm and a roughness of about 0.1 μm.

To assess the optical characteristics of the resulting thin films of pure titania and its Sc-doped counterparts, the materials were inkjet-printed onto silicon wafers and then characterized by specular reflectance UV-vis spectroscopy, the results of which are shown in Figure 6c. The presence of Sc dopants in the thin films shifted the absorbance maximum from 366 nm for pure TiO_2 to 425 nm for 10 wt.% Sc-TiO_2.
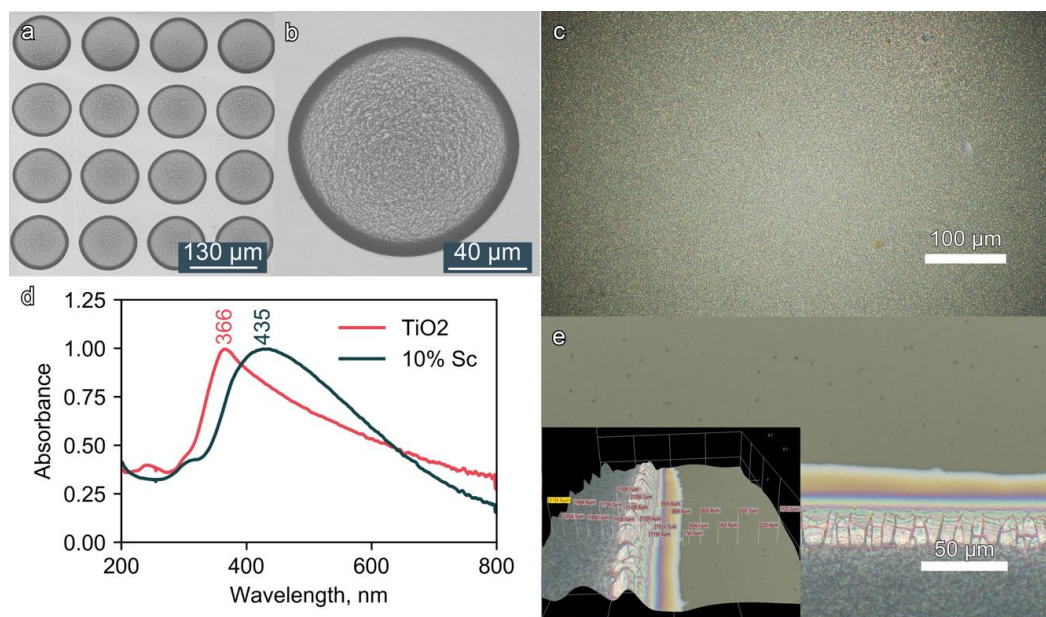
Figure 6. SEM images of a printed drop array (**a**) and single drop (**b**) of Sc-doped titania; optical microscope images of the central part (**c**) and edge (**e**) of the printed film (inset—film profile); optical absorbance spectra of the printed films of pure and 10% Sc-doped titania (**d**).

4. Conclusions

In this work, a sol–gel methodology was employed as a facile and scalable technique enabling the reproducible deposition of well-defined Sc-doped TiO_2 nanoparticles with Sc lattice contents up to 10 wt.% onto solid supports. XRD and EDX measurements confirmed the formation of a fully homogeneous phase of doped anatase nanoparticles. UV-vis spectroscopy evidenced a significant boost of the optical absorbance along with a pronounced shift of the bandgap to the visible area of the spectrum. To demonstrate the high efficiency of such materials for practical applications, we optimized the rheological parameters of Sc-TiO_2 colloid for inkjet printing. Uniform drop arrays were generated using this ink and characterized with UV-vis spectroscopy. The results show the high consistency of the characteristics of the thin films with those obtained of the bulk material. We anticipate that the described approach and the presented results will assist in future research on optically enhanced materials and their integration in modern industrial applications.

Supplementary Materials: The following are available online at http://www.mdpi.com/2079-6412/9/2/78/s1, Video S1: Stable droplet generation.

Author Contributions: Conceptualization: A.M., A.K., and A.V.V.; Data curation: A.M., A.V.V., and E.A.P.; Formal analysis: K.K., E.V.K., and V.S.; Investigation: K.K., E.V.K., and V.S.; Methodology: K.K., E.V.K., and V.S.; Software: E.V.K.; Supervision: A.V.V. and E.A.P.; Validation: K.K. and V.S.; Visualization: K.K., E.V.K., and V.S.; Writing—original draft: K.K., E.V.K., and V.S.; Writing—review and editing: A.V.V. and E.A.P.

Funding: This work was supported by the Russian Science Foundation (No. 16-19-10346).

Acknowledgments: The authors are grateful to Danilovich D.P. and Perevislov S.N. for their comprehensive support, to the engineering center of St. Petersburg Technological Institute for research assistance with XRD measurements, and to Inna Popov (Hebrew University of Jerusalem) for performing TEM measurements. Partial support from the Ministry of Education and Science of Russian Federation (Project 11.1706.2017/4.6) is acknowledged. The Netherlands Organization for Scientific Research (NWO) and surfSARA are acknowledged for providing access to their supercomputer facilities.

Conflicts of Interest: The authors declare no conflict of interest. The funders had no role in the design of the study; in the collection, analyses, or interpretation of data; in the writing of the manuscript, or in the decision to publish the results.

Appendix A

Spin-polarized periodic DFT calculations were performed using density functional theory (DFT) as implemented in VASP 5.2 code [39]. The Perdew–Burke–Ernzerhof functional was supplemented by the "+U" description proposed by Perdew et al. [40] and Dudarev et al. [41]. The Hubbard (U) parameter of on-site d-electrons correction was set equal to 9.3 eV for both Ti and Sc. [42] All calculations were performed using the projector augmented wave (PAW) [43,44] with a cutoff energy of 450 eV. The Brillouin zone was sampled with $2 \times 2 \times 2$ gamma-centered k-points mesh. The systems convergence was assumed when the acting forces were less than 0.03 eV/Å.
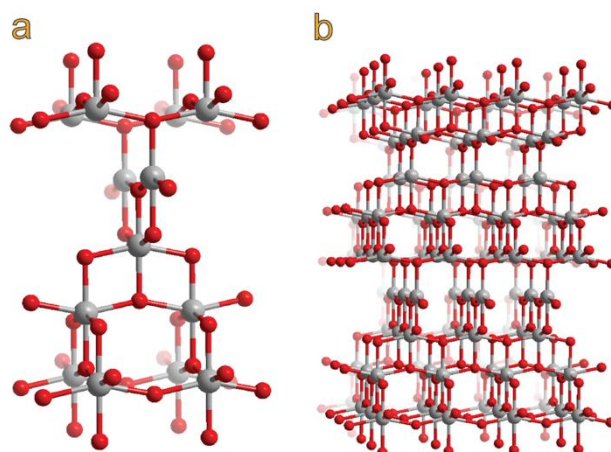
Figure A1.　　Anatase models optimized at the PBE + U level of theory:　　unit cell (**a**) and $3 \times 3 \times 2$ supercell (**b**); oxygen atoms are red, titanium atoms are grey.
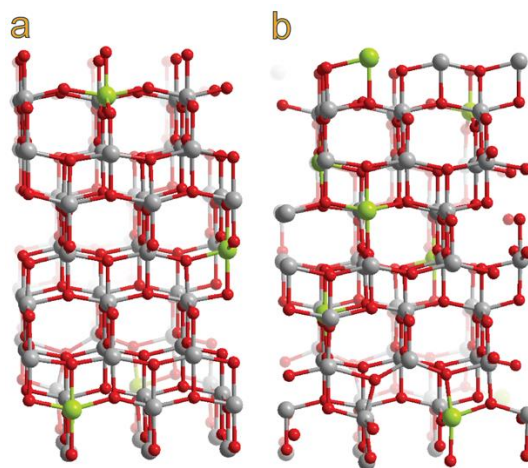
Figure A2. Sc-doped anatase ($3 \times 3 \times 2$) supercell models corresponding to 5 wt.% (**a**) and 10 wt.% (**b**) Sc^{3+} optimized at the PBE + U level of theory.
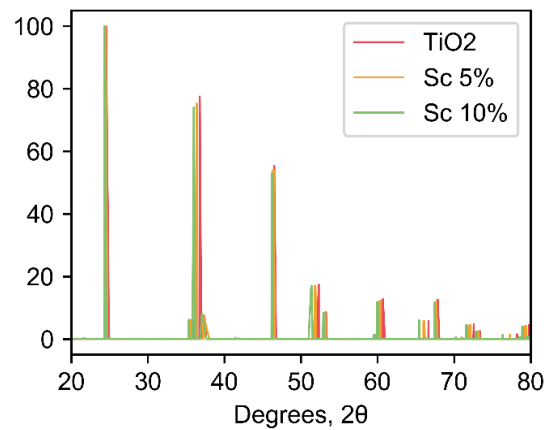
Figure A3. Powder diffraction pattern of pure and Sc-doped anatase simulated by VESTA code. The wavelength of the source was 1.54187 Å.

Formally, unless extreme conditions are imposed, doping with metal ions having a valence lower than that of Ti^{4+} generates a charge imbalance that can be compensated by the formation of an oxygen vacancy and the reduction of a neighboring Ti^{4+} to the Ti^{3+} state [45,46]. Such defects represent the most basic type of defects in the crystal lattice and the process of their formation is illustrated schematically in Figure 3. Such oxygen vacancies give rise to new electronic states localized between the conduction and valence bands. The partially occupied d-orbitals of the inserted Ti^{3+} bring new donor states generated as a result of the electron redistribution in the vicinity of the reduced Ti atoms. These new donor states affect the electronic structure of TiO_2. They might overlap with band edges, creating a bandgap alteration in Sc-TiO_2 materials [47].
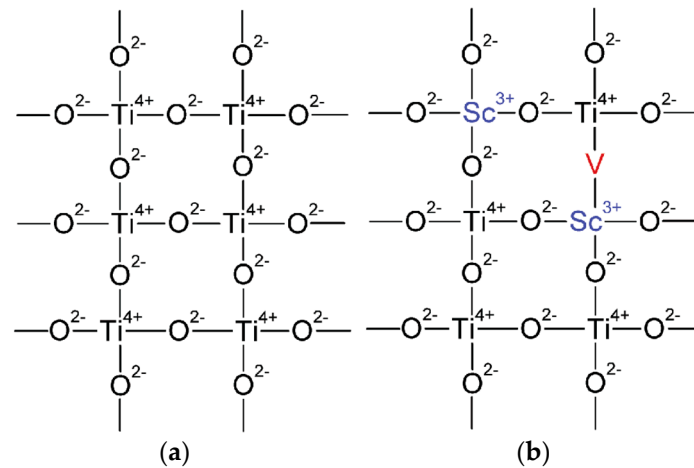
Figure A4. A schematic illustration of (**a**) TiO_2 and (**b**) Sc-TiO_2 lattices with oxygen vacancies (V) indicated.

To evaluate the thermodynamics of the Sc doping process, the energy of Sc defect formation was calculated in two different ways (Equations (A1) and (A2)). Equation (A1) corresponds to the energy of the point defects in the Sc-doped TiO_2 composite formed from the elemental phases of Ti and Sc.

$$E_f \text{ (Sc)} = (E_{Sc\text{-doped}} - E_{undoped} + n\mu_{Ti} - m\mu_{Sc} + k\mu_o)/m \tag{A1}$$

where $E_{Sc\text{-doped}}$ is the energy of the Sc-doped anatase, $E_{undoped}$ is the energy of pure anatase, μTi is a chemical potential of the Ti element obtained from the *hcp* Ti bulk metal, μSc is a chemical potential computed from the *hcp* Sc bulk metal, and μ_o is the chemical potential of the O atom calculated from

the total energy of an oxygen molecule. The values of *n*, *m*, and *k* correspond to the numbers of Ti, Sc, and O atoms removed or inserted into a TiO_2 supercell.

Equation (A2) corresponds to the energy insertion into the TiO_2 structures which are formed from the elemental phases of Ti and Sc.

Equation (A2) reflects the defect formation energy in the Sc-doped structure obtained from the phases of Sc_2O_3 and TiO_2 oxides:

$$E_f \text{ (Sc)}= (E_{Sc\text{-}doped} - E_{undoped} + s\mu TiO_2 - t\mu Sc_2O_3)/t \tag{A2}$$

where μTiO_2 is the chemical potential of the TiO_2 unit cell. μSc_2O_3 is the chemical potential of the Sc_2O_3 unit cell. The values of *s* and *t* are coefficients of removed or inserted Ti and Sc atoms.

Table A1. Formation energies and corresponding bandgap of pure and Sc-doped TiO_2.

Sc-Doped System, %	E_f, eV/atom from Elemental Phase	E_f, eV/atom from Oxide Phase
0	—	
5	2.00	1.47
10	1.96	1.42

Table A2. Lattice parameters of pure and Sc-doped TiO_2.

Sc-Doped Anatase, %	Lattice Parameters, Å		
	a	*b*	*c*
0%	11.72	11.72	19.58
5%	11.74	11.76	19.75
10%	11.76	11.79	19.96

Table A3. Results of BET and BJH analyses.

Sample	Specific Surface Area, m²/g	Volume of Pores, cm³/g	Radius of Pores, Å
Pure TiO_2	146.028	0.007	17.239
3% Sc-TiO_2	159.981	0.006	17.244
5% Sc-TiO_2	167.464	0.010	17.271
7% Sc-TiO_2	172.451	0.008	17.305
10% Sc-TiO_2	176.145	0.007	17.477
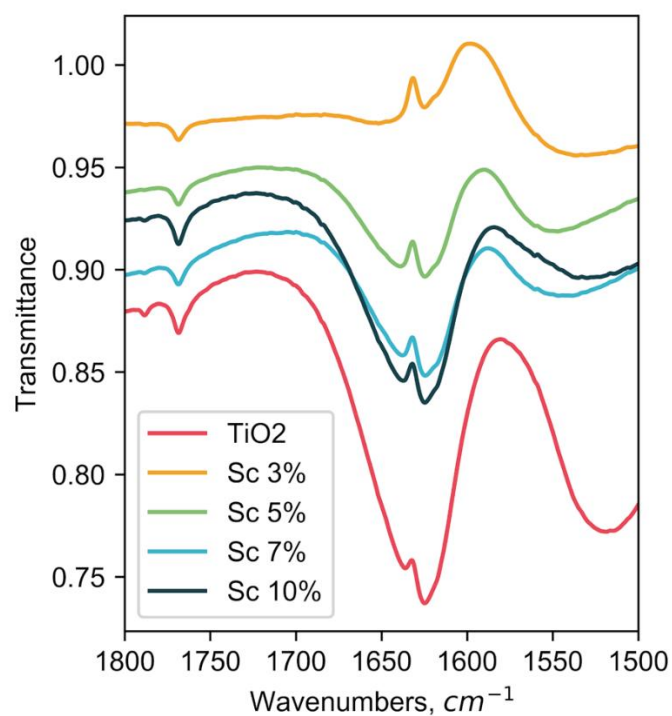
Figure A5. IR spectra of synthesized samples.
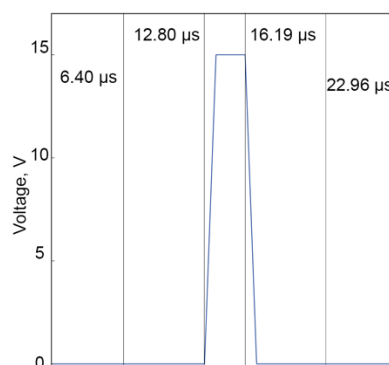
Figure A6. Waveform (voltage curve) of inkjet printing system.
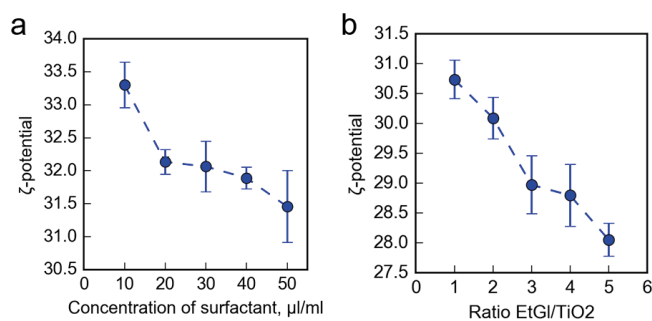
Figure A7. Zeta potential of inks with the addition of a surfactant (**a**) and ethylene glycol (**b**).

References

1. Zhang, Q.; Uchaker, E.; Candelaria, S.L.; Cao, G. Nanomaterials for energy conversion and storage. *Chem. Soc. Rev.* **2013**, *42*, 3127. [CrossRef] [PubMed]
2. Chen, G.; Seo, J.; Yang, C.; Prasad, P.N. Nanochemistry and nanomaterials for photovoltaics. *Chem. Soc. Rev.* **2013**, *42*, 8304. [CrossRef] [PubMed]

3. Adly, N.; Feng, L.; Krause, K.J.; Mayer, D.; Yakushenko, A.; Offenhäusser, A.; Wolfrum, B. Flexible Microgap Electrodes by Direct Inkjet Printing for Biosensing Application. *Adv. Biosys.* **2017**, *1*, 1600016. [CrossRef]

4. Bai, L.; Xie, Z.; Wang, W.; Yuan, C.; Zhao, Y.; Mu, Z.; Zhong, Q.; Gu, Z. Bio-Inspired Vapor-Responsive Colloidal Photonic Crystal Patterns by Inkjet Printing. *ACS Nano* **2014**, *8*, 11094–11100. [CrossRef] [PubMed]

5. Chen, C.-T. Inkjet Printing of Microcomponents: Theory, Design, Characteristics and Applications. In *Features of Liquid Crystal Display Materials and Processes*; Kamanina, N., Ed.; InTech: Rijeka, Croatia, 2011.

6. Singh, M.; Haverinen, H.M.; Dhagat, P.; Jabbour, G.E. Inkjet printing-process and its applications. *Adv. Mater.* **2010**, *22*, 673–685. [CrossRef] [PubMed]

7. Hebner, T.R.; Wu, C.C.; Marcy, D.; Lu, M.H.; Sturm, J.C. Inkjet printing of doped polymers for organic light emitting devices. *Appl. Phys. Lett.* **1998**, *72*, 519–521. [CrossRef]

8. De Gans, B.-J.; Duineveld, P.C.; Schubert, U.S. Inkjet printing of polymers: state of the art and future developments. *Adv. Mater.* **2004**, *16*, 203–213. [CrossRef]

9. De Gans, B.-J.; Schubert, U.S. Inkjet printing of well-defined polymer dots and arrays. *Langmuir* **2004**, *20*, 7789–7793. [CrossRef]

10. Yakovlev, A.V.; Milichko, V.A.; Vinogradov, V.V.; Vinogradov, A.V. Inkjet color printing by interference nanostructures. *ACS Nano* **2016**, *10*, 3078–3086. [CrossRef]

11. Yakovlev, A.V.; Pidko, E.A.; Vinogradov, A.V. Inkjet printing of transparent sol-gel computer generated holograms. *Opt. Mater. Express* **2016**, *6*, 3794. [CrossRef]

12. Keller, K.; Yakovlev, A.V.; Grachova, E.V.; Vinogradov, A.V. Inkjet printing of multicolor daylight visible opal holography. *Adv. Funct. Mater.* **2018**, *28*, 1706903. [CrossRef]

13. Gao, M.; Li, L.; Song, Y. Inkjet printing wearable electronic devices. *J. Mater. Chem. C* **2017**, *5*, 2971–2993. [CrossRef]

14. Cummins, G.; Desmulliez, M.P.Y. Inkjet printing of conductive materials: a review. *Circuit World* **2012**, *38*, 193–213. [CrossRef]

15. Sum, T.C.; Mathews, N. Advancements in perovskite solar cells: photophysics behind the photovoltaics. *Energy Environ. Sci.* **2014**, *7*, 2518–2534. [CrossRef]

16. Zhang, H.; Yang, Z.; Zhang, X.; Mao, N. Photocatalytic effects of wool fibers modified with solely TiO_2 nanoparticles and N-doped TiO_2 nanoparticles by using hydrothermal method. *Chem. Eng. J.* **2014**, *254*, 106–114. [CrossRef]

17. Long, R.; English, N.J. Band gap engineering of (N,Ta)-codoped TiO_2: A first-principles calculation. *Chem. Phys. Letter.* **2009**, *478*, 175–179. [CrossRef]

18. Zhang, G.; Liu, G.; Wang, L.; Irvine, J.T.S. Inorganic perovskite photocatalysts for solar energy utilization. *Chem. Soc. Rev.* **2016**, *45*, 5951–5984. [CrossRef]

19. Toroker, M.C.; Carter, E.A. Transition metal oxide alloys as potential solar energy conversion materials. *J. Mat. Chem. A* **2013**, *1*, 2474. [CrossRef]

20. Wang, M.; Ioccozia, J.; Sun, L.; Lin, C.; Lin, Z. Inorganic-modified semiconductor TiO_2 nanotube arrays for photocatalysis. *Energy Environ. Sci.* **2014**, *7*, 2182–2202. [CrossRef]

21. Hanaor, D.A.H.; Assadi, M.H.N.; Li, S.; Yu, A.; Sorrell, C.C. Ab initio study of phase stability in doped TiO_2. *Comput. Mech.* **2012**, *50*, 185–194. [CrossRef]

22. Seebauer, E.G.; Kratzer, M.C. *Charged Semiconductor Defects: Structure, Thermodynamics and Diffusion*; Springer: London, UK, 2009.

23. Pan, X.; Yang, M.-Q.; Fu, X.; Zhang, N.; Xu, Y.-J. Defective TiO_2 with oxygen vacancies: synthesis, properties and photocatalytic applications. *Nanoscale* **2013**, *5*, 3601. [CrossRef] [PubMed]

24. Liu, K.; Litke, A.; Su, Y.; van Campenhout, B.G.; Pidko, E.A.; Hensen, E.J.M. Photocatalytic decarboxylation of lactic acid by Pt/TiO_2. *Chem. Commun.* **2016**, *52*, 11634–11637. [CrossRef] [PubMed]

25. Kang, Y.S.; Zhang, D.R. Synthesis and characterization of titanium dioxide doped with Sc^{3+} ions. *Int. J. Nanosci.* **2006**, *5*, 351–357. [CrossRef]

26. Zhang, D.R.; Kang, Y.S. Synthesis and Characterization of Nanocrystalline TiO2 Doped with 2 at.% Sc^{3+} and V^{5+} Ions. *Solid State Phenom.* **2007**, *121–123*, 41–44. [CrossRef]

27. Pan, J.W.; Li, C.; Zhao, Y.F.; Liu, R.X.; Gong, Y.Y.; Niu, L.Y.; Liu, X.J.; Chi, B.Q. Electronic properties of TiO_2 doped with Sc, Y, La, Zr, Hf, V, Nb and Ta. *Chem. Phys. Lett.* **2015**, *628*, 43–48. [CrossRef]

28. Cavalheiro, A.A.; Bruno, J.C.; Saeki, M.J.; Valente, J.P.S.; Florentino, A.O. Effect of scandium on the structural and photocatalytic properties of titanium dioxide thin films. *J. Mater. Sci.* **2008**, *43*, 602–608. [CrossRef]

29. Tao, Z.; Le Borgne, B.; Mohammed-Brahim, T.; Jacques, E.; Harnois, M. Spreading and drying impact on printed pattern accuracy due to phase separation of a colloidal ink. *Colloid Polym. Sci.* **2018**, *296*, 1749–1758. [CrossRef]

30. Klestova, A.; Cheplagin, N.; Keller, K.; Slabov, V.; Zaretskaya, G.; Vinogradov, A.V. Inkjet printing of optical waveguides for single-mode operation. *Adv. Opt. Mat.* **2019**, *7*, 1801113. [CrossRef]

31. Slabov, V.; Vinogradov, A.V.; Yakovlev, A.V. Inkjet printing of specular holograms based on a coffee-ring effect concave structure. *J. Mat. Chem. C* **2018**, *6*, 5269–5277. [CrossRef]

32. Yakovlev, A.V.; Milichko, V.A.; Pidko, E.A.; Vinogradov, V.V.; Vinogradov, A.V. Inkjet printing of TiO2/AlOOH heterostructures for the formation of interference color images with high optical visibility. *Sci. Rep.* **2016**, *6*, 37090. [CrossRef]

33. Safaryan, S.M.; Yakovlev, A.V.; Vinogradov, A.V.; Vinogradov, V.V. Inkjet printing of the chromogen free oxidase based optical biosensors. *Sensor. Actuat. B Chem.* **2017**, *251*, 746–752. [CrossRef]

34. Banisharif, A.; Khodadadi, A.A.; Mortazavi, Y.; Anaraki Firooz, A.; Beheshtian, J.; Agah, S.; Menbari, S. Highly active Fe_2O_3-doped TiO_2 photocatalyst for degradation of trichloroethylene in air under UV and visible light irradiation: Experimental and computational studies. *Appl. Catal. B Environ.* **2015**, *165*, 209–221. [CrossRef]

35. Momma, K.; Izumi, F. *VESTA 3* for three-dimensional visualization of crystal, volumetric and morphology data. *J. Appl. Crystallogr.* **2011**, *44*, 1272–1276. [CrossRef]

36. Tauc, J.; Grigorovici, R.; Vancu, A. Optical properties and electronic structure of amorphous germanium. *Phys. Status Solidi* **1966**, *15*, 627–637. [CrossRef]

37. Davis, E.A.; Mott, N.F. Conduction in non-crystalline systems V. Conductivity, optical absorption and photoconductivity in amorphous semiconductors. *Phil. Mag.* **1970**, *22*, 903–922. [CrossRef]

38. Dette, C.; Pérez-Osorio, M.A.; Kley, C.S.; Punke, P.; Patrick, C.E.; Jacobson, P.; Giustino, F.; Jung, S.J.; Kern, K. TiO_2 Anatase with a Bandgap in the Visible Region. *Nano Lett.* **2014**, *14*, 6533–6538. [CrossRef] [PubMed]

39. Kresse, G.; Furthmüller, J. Efficient iterative schemes for *ab initio* total-energy calculations using a plane-wave basis set. *Phys. Rev. B* **1996**, *54*, 11169–11186. [CrossRef]

40. Perdew, J.P.; Burke, K.; Ernzerhof, M. Generalized gradient approximation made simple. *Phys. Rev. Lett.* **1996**, *77*, 3865. [CrossRef]

41. Dudarev, S.L.; Botton, G.A.; Savrasov, S.Y.; Humphreys, C.J.; Sutton, A.P. Electron-energy-loss spectra and the structural stability of nickel oxide: An LSDA+U study. *Phys. Rev. B* **1998**, *57*, 1505–1509. [CrossRef]

42. Zhu, H.X.; Zhou, P.X.; Li, X.; Liu, J.-M. Electronic structures and optical properties of rutile TiO_2 with different point defects from DFT+U calculations. *Phys. Lett. A* **2014**, *378*, 2719–2724. [CrossRef]

43. Kresse, G.; Joubert, D. From ultrasoft pseudopotentials to the projector augmented-wave method. *Phys. Rev. B* **1999**, *59*, 1758–1775. [CrossRef]

44. Blöchl, P.E. Projector augmented-wave method. *Phys. Rev. B* **1994**, *50*, 17953–17979. [CrossRef]

45. Nowotny, M.K.; Sheppard, L.R.; Bak, T.; Nowotny, J. Defect Chemistry of Titanium Dioxide. Application of Defect Engineering in Processing of TiO_2-Based Photocatalysts. *J. Phys. Chem. C* **2008**, *112*, 5275–5300. [CrossRef]

46. Wendt, S.; Schaub, R.; Matthiesen, J.; Vestergaard, E.K.; Wahlström, E.; Rasmussen, M.D.; Thostrup, P.; Molina, L.M.; Lægsgaard, E.; Stensgaard, I.; et al. Oxygen vacancies on TiO_2(110) and their interaction with H2O and O2: A combined high-resolution STM and DFT study. *Surf. Sci.* **2005**, *598*, 226–245. [CrossRef]

47. Roose, B.; Pathak, S.; Steiner, U. Doping of TiO_2 for sensitized solar cells. *Chem. Soc. Rev.* **2015**, *44*, 8326–8349. [CrossRef] [PubMed]